

Landslides (2020) 17:1191–1206
 DOI 10.1007/s10346-020-01358-x
 Received: 3 November 2019
 Accepted: 21 January 2020
 Published online: 7 February 2020
 © Springer-Verlag GmbH Germany
 part of Springer Nature 2020

Yan Yan · Yifei Cui · Xin Tian · Sheng Hu · Jian Guo · Ziang Wang · Shuyao Yin · Liufeng Liao

Seismic signal recognition and interpretation of the 2019 “7.23” Shuicheng landslide by seismogram stations

Abstract A systematic study of the physical and mechanical processes of landslide development and evolution is important for forecasting, early warning, and prevention of landslide hazards. In the absence of on-site monitoring data, seismic networks can be employed to continuously record ground seismicity generated during landslides. However, landslide seismic signals are relatively weak and inevitably affected by noise interference. Furthermore, systematic characterization and reconstruction of the landslide evolution process remain poorly reported. An evaluation method to recognize landslide events based on seismic signal characteristics is therefore important. This study analyzes the 2019 “7.23” Shuicheng landslide based on data from nearby seismic stations. A landslide seismic signal recognition method is developed based on short-time Fourier transform (STFT) and band-pass filter (BP-filter) analysis. Data from 14 stations near the landslide were reviewed and the landslide data from one station was selected for analysis. The landslide seismic signal was noise-attenuated by using the empirical mode decomposition (EMD) and BP-filter methods. Fast Fourier transform (FFT), STFT, and power spectral density analyses were applied to the landslide seismic signal with higher signal-to-noise ratio (SNR) to obtain the time–frequency signal characteristics of the landslide process. Finally, combined with landslide field survey data, the dynamic process of the landslide was reconstructed based on the seismic signal, and the landslide was divided into four stages: the fracture-transition stage, the accelerated initiation stage, the bifurcation-scraping stage, and the deposition stage. The dynamic characteristics of each stage of the landslide are presented. The results indicate that the initial fracture point of the landslide is located between the bottom of the sliding source area and the top of the acceleration zone, not as traditionally thought, at the top of the sliding source area; this would be difficult to determine through field survey and analysis only. These results provide theoretical guidance for the study of seismic signal extraction, identification of landslide dynamic parameters, and characterization and reconstruction of landslide processes.

Keywords Seismic network · Shuicheng landslide · Signal extraction and recognition · Signal interpretation · Landslide process reconstruction

Introduction

Landslides are a geological phenomenon in which the slope rock and soil body slip along a shear failure surface. Landslides are classified as major geological hazards by many countries worldwide and are characterized by extensive damage under difficult monitoring and control conditions (Aleotti and Chowdhury 1999; Yesilnacar and Topal 2005; Chen et al. 2013; Hungr et al. 2014; Zhou et al. 2016; Cui et al. 2017; Ouyang et al. 2017). Landslide hazards have caused major property damage and safety concerns (Cui et al.

2009; Huang 2009; Zhou et al. 2013a; Schimmel and Hübl 2016; Sheng et al. 2018; Cui et al. 2019; Ouyang et al. 2019). Systematic research on the physical and mechanical processes of landslide evolution and sliding is therefore of great significance for the forecast, early warning, and prevention of landslide hazards.

It is necessary to conduct on-site monitoring of potential landslides to understand the motion and deformation characteristics of the various stages of a landslide (Yamada et al. 2013). However, owing to the strong destructive nature of landslide hazards, on-site monitoring equipment is often damaged, which makes monitoring data difficult to collect (Guo et al. 2020). Direct observation data, therefore, mostly come from the occurrence of landslides while in situ observations are relatively scarce. The lack of direct observation data is a key factor limiting the study of landslide physical processes (Yamada et al. 2013; Zhou et al. 2013b; Li et al. 2017; Huang et al. 2018). In response to the above problems, many studies have proposed the use of seismic monitoring to obtain data on landslide evolution. Seismic networks can continuously record ground seismicity generated during landslide occurrence; therefore, seismic signals can be studied to obtain the dynamic landslide characteristics (Yamada et al. 2012; Chen et al. 2013; Petley 2013; Yamada et al. 2013; Lin 2015; Hibert et al. 2017; Li et al. 2017).

In recent years, seismic methods have received increasing attention because of their potential to monitor hazards remotely (Helmstetter and Garambois 2010; Moretti et al. 2012; Ekström and Stark 2013; Moore et al. 2017; Guinau et al. 2019). Seismic signal analysis can quickly determine the time, location, and scale of a landslide; moreover, the seismic mode and corresponding dynamic process of the landslide can be investigated to provide a basis for early warning of landslide hazards (Kao et al. 2012; Sakals et al. 2012; Lombardo et al. 2019; Zhang et al. 2019). In recent years, spectrum analysis of seismic signals has been widely used in the study of landslide characteristics (Moretti et al. 2012; Levy et al. 2015; Ogiso and Yomogida 2015). These studies found that seismic signals generated by landslides can be divided into high- and low-frequency signals, both of which can provide information regarding the landslide dynamic characteristics (Vilajosana et al. 2008; Chen et al. 2013; Hibert et al. 2014; Li et al. 2017). However, high-frequency signals are more complex and attenuate rapidly so it is difficult to analyze the properties of landslide volume, velocity, and trajectory based on these signals (Huang et al. 2007; Allstadt 2013; Dammeyer et al. 2016; Fuchs et al. 2018; Zhang et al. 2019). Current common practice, therefore, is to invert the long period signal on the basis of observational data to first obtain the force–time function of the landslide (Brodsky et al. 2003; Favreau et al. 2010; Schneider et al. 2010), and then quantitatively obtain the landslide kinematic parameters (Sakals et al. 2012; Feng et al. 2017; Fuchs et al. 2018; Kuo et al. 2018; Zhang et al. 2019).

Overall, some progress has been made in the study of landslide seismic signals but many challenges remain in signal identification

(Zhao et al. 2015; Fuchs et al. 2018). For example, landslide seismic signals are relatively weak and inevitably affected by noise interference during signal collection, such as the noise generated by accompanying earthquake events. Higher-amplitude noise tends to obscure the landslide seismic signals. Effective identification of landslide seismic signals is therefore of great importance. Some recent studies have also explored signal interference (Helmstetter and Garambois 2010; Feng, 2011; Sheng et al. 2018). These methods can effectively overcome the challenges introduced by signal noise pollution. However, systematic characterization and reconstruction of landslide processes is still inadequate. It is therefore important to establish an efficient landslide event assessment method based on the characteristics of seismic signals.

This study is based on the “7.23” Shuicheng landslide that occurred in 2019. Seismic signal data collected by nearby seismic stations were initially processed and screened by using the short-time Fourier transform (STFT) and band-pass filter (BP-filter) methods to identify and extract the landslide-induced signal. The landslide field survey data were then processed using empirical mode decomposition (EMD), fast Fourier transform (FFT), STFT, and power spectral density (PSD) analysis to obtain the signal time–frequency characteristics of the landslide. The landslide process was reconstructed with the dynamic characteristics analyzed at each stage. This study provides important information for the extraction of seismic signals to identify landslide dynamic parameters and characterize and reconstruct landslide processes.

Study area

Geologic and topographic conditions

The landslide studied here is located in the town of Jichang in southwestern Shuicheng County in western Guizhou Province, China (Fig. 1a and b), situated in the watershed of the Pearl and Yangtze river basins.

From the perspective of regional tectonics, the landslide is located at the interface between the southeastern margin of the Qinghai-Tibet Plateau and the South China Block. Therefore, the regional structural morphology and lithological combinations are complex. The geological map of the Shuicheng landslide area is shown in Fig. 2. The surface strata at the landslide comprise mainly Permian Emeishan basalts and basalt lavas, interspersed with volcanic clastic rocks, sunken volcanic clastic rocks, and coal-containing clastic rocks (Li et al. 2019; Xu et al. 2019). The basalt is not very weather resistant, and a thick layer of loose volcanic soil is widespread in the gradually sloping area, providing good conditions for farming. There are more villages at the relatively flat area at the foot of the slope and intensive farming has increased the rock weathering in the area, forming a thicker soil layer. This has led to poor stability of the ground surface and increased landslide risk. The landslide is located in the Yangtze platform in the northern part of the Qianbei-Tailong-Liupanshui fault depression in the middle of the westward tectonic deformation zone, the north of the Jinan knob tectonic deformation zone and the southeast of the northeast of the Zongyi fault arch in the Qianbei platform, along the southwest border of the tectonic deformation zone. The activity of the fault zone in the late Quaternary was very strong, with many strong historical earthquakes of magnitude 7 or higher not showed in the area shown in Fig. 2, but to the west of the area (Xu et al. 2019). The surrounding faults are mainly Early-

Middle Pleistocene faults, and some have been recently active, generating moderately strong earthquakes of about magnitude 5 (Fig. 2). However, no active faults have developed near the landslide area (Xu et al. 2019). The folds and faults are crisscrossed in the area, and the strata are strongly affected by structural breaks. The rock mass is very fragmented, and the geological structure is complex, characterized by large terrain fluctuations, mountains with sharp topographic features, and karst development. The easily weathered surface lithology coupled with tectonic-induced fragmentation and strong weathering caused by high and steep terrain in the later stage makes the area more prone to geological hazards (Si et al. 2012).

Climate and rainfall characteristics

Rainfall in Shuicheng County occurs mainly between May and September, accounting for 50% of the annual rainfall. Moreover, 78.5% of the hazardous geological events in the area occurred during this five-month period (Fig. 3), showing a high correlation between the number of geological hazard events and rainfall.

Meteorological data indicate extensive rain in the month prior to the Jichang landslide. The accumulated rainfall from the beginning of July in Shuicheng County reached 288.9 mm. During the six-day period before the landslide (July 18 to 23), there were three heavy rainfall events of 43.1, 45.2, and 47.8 mm, and a light rain that started at 8:00 PM on July 23 and ended at 7:00 AM on July 24 with a total precipitation of 5.5 mm (Fig. 3b). The results show that the rainfall 7 days before the occurrence of the landslide is 70.14 mm.

The “7.23” Shuicheng landslide event

Pre- and post-landslide characteristics

According to DEM measurements, the landslide body is 415 m long and 207 m wide with an area of about $8.6 \times 10^4 \text{ m}^2$ and an average sliding depth of about 20 m. According to this estimation, the volume of the landslide body is about $172 \times 10^4 \text{ m}^3$.

The orthophoto data clearly indicate that the landslide area is roughly rectangular, trending NNE. There were three roads (A, B, and C) on the surface of the landslide mass before the sliding event, with a gentle platform on the leading edge between Roads B and C (Figs. 4a and 3b). The front edges of Roads A and C and the platform are separated by different areas of the landslide section. Road A runs through the sliding source zone. The front edge and platform of the source zone are the acceleration zone, adjacent to the platform and Road C. The area between the scraper area and Road C is the sediment-impact zone (Fig. 4c).

Sliding source zone (I)

The sliding source area is located above Road A. The landslide surface has an inclination angle of 37° , strike of 20° , width of about 162 m, and a maximum elevation difference of 74 m. At the top of the landslide body, basaltic foundation rocks are exposed and have clear scratches (Fig. 4d). Soil and vegetation from the top of the sliding source zone have accumulated between the central part of the sliding source area and Road A. The vegetation in this area is randomly distributed (Fig. 4e); the roof of a house, originally at the top of the source zone, is relatively intact, and the sides of the landslide are inclined towards the landslide center. After the landslide, continuous rain fell in the nearby farming town and a

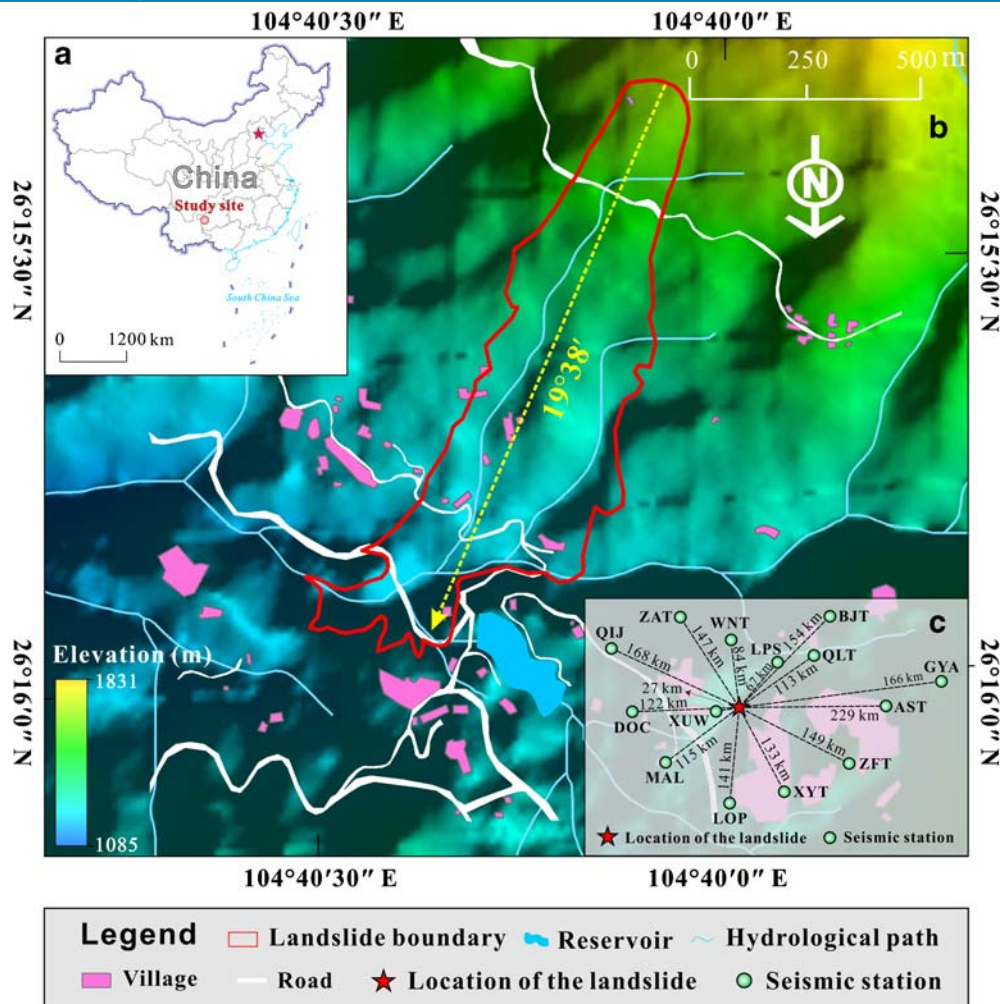


Fig. 1 Geologic and topographic features of the Shuicheng landslide. (This figure is based on the standard map of GS (2019) 1651, which is downloaded from the Standard Map Service website of the National Surveying and Mapping Geographic Information Bureau of China. The base map has no modification.) a Location of the Jichang landslide in Shuicheng County, Liupanshui City, Guizhou Province. b DEM of the pre-landslide area. c Position of the seismic stations relative to the landslide

number of clear water catchments formed on the landslide surface (Fig. 4d). The catch trace clearly indicates that an unstable zone developed along the slope direction before the landslide occurred.

Acceleration zone (II)

This area is between Roads A and B. Figure 4a shows that before the landslide event, a relatively gentle platform is present 80 m below Road A (Fig. 4a). The gentle platform and Road A are relatively steep with a slope of about 39°. The slope between the wide platform and Road B is shallower. The gentle platform gradually evolves downward into a ridge-like gentle slope, joining with the tail slope of Road B.

Debris motion zone (III)

This area is divided into two parts by a central ridge that did not undergo significant sliding and is bordered by valleys to the east and west that were severely affected by the landslide (Fig. 4f). With its high elevation, the central ridge was not directly affected by the landslide. The valley to the east of the ridge was the most severely affected area. The eastern landslide is about 630 m long, straight,

and wide, with an average slope of 19.5° with a gradient of 353‰, which is favorable for landslide development. The landslide body is 10–20 m high and strongly eroded. The west side of the valley is deeper and steeper than the east side, with an average depth of 30 m. No houses are found on either side of the valley. Dry valleys occur about halfway between Roads B and C where the valley's orientation turns eastward 30°. After the slide, the landslide body piled up over the ridge on the east side of the valley. After deposition of ~15 m of sediment, the two houses built on Road C were completely buried.

Sediment zone (IV)

The accumulation area is mainly located in the gently sloping area of Road C. It is distributed as adjacent segments. The distance between the northern and southern edges of the zone is about 220 m, the distance between its east and west edges is about 200 m, and the area covers about $4.3 \times 10^4 \text{ m}^2$. A 6-m-high two-story house is still standing on the east side of the sedimentary area. Most of the landslide body was deposited at an altitude of about 1150 m. The elevation of the front end of the sedimentary zone is

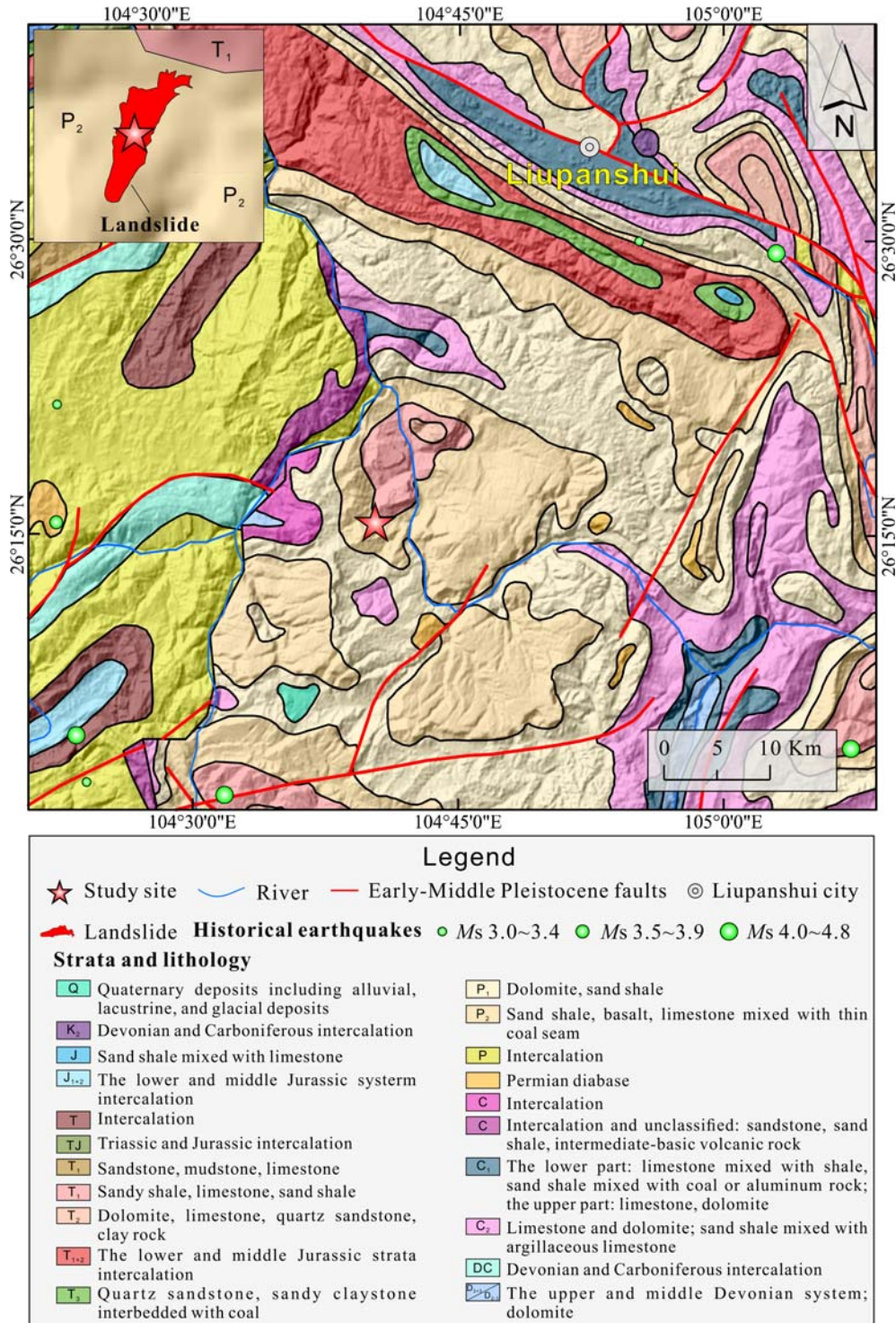


Fig. 2 Geological map of the Shuicheng landslide area

about 1193 m. The toe of the landslide body is claw-shaped with clear impact marks (Fig. 4f).

Ground-motion records and signals

Evidence from local residents indicates that the start time of the landslide was about 21:20 on July 23, 2019, Beijing time

(13:20 UTC time) and the event lasted about 3 to 4 min. Jichang is located in southern Shuicheng County, Guizhou Province, at the junction of three counties in Yunnan and Guizhou. There are 14 seismic stations in Guizhou and Yunnan Province located within 200 km of the landslide point (Fig. 1c).

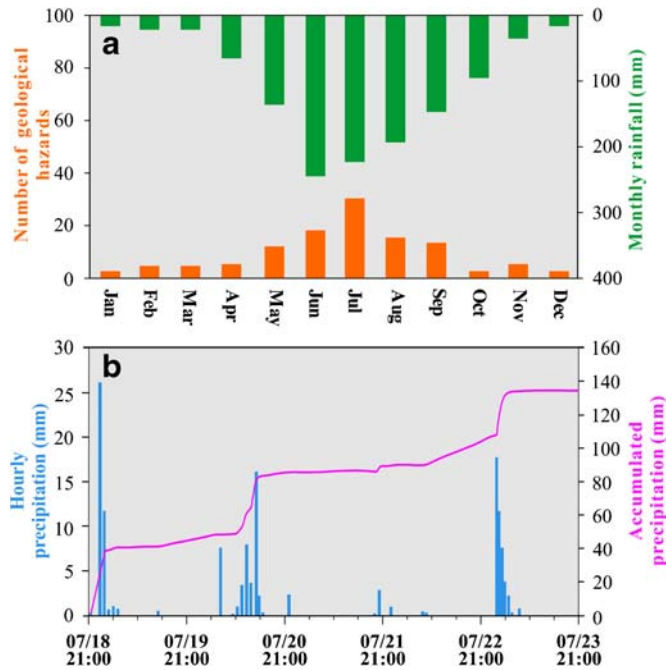


Fig. 3 Rainfall characteristics of the Shuicheng landslide. **a** Relationship between average monthly rainfall and occurrence of new geological hazards. **b** Hourly precipitation in Jichang town from July 18 to 23, 2019 (data from the Ecological Meteorology and Satellite Remote Sensing Center of Guizhou Province)

Methodology

The scale, displacement, and crustal seismicity of the landslide are relatively small. Residents near the landslide mistakenly thought that the landslide was fireworks or a small earthquake. The surface lithology of this area is basalt, which can weather easily and forms a thick loose surface layer with relatively strong absorption attenuation. These factors make the seismic signal of this landslide recorded by each station relatively weak and its identification more difficult. For this reason, we developed a weak signal processing and analysis process (Fig. 5).

Empirical mode decomposition

In theory, EMD can effectively decompose any type of signal. EMD can adaptively separate the nonlinear non-stationary seismic signals caused by a landslide and analyze each component separately, which can accurately reflect the energy (or frequency) in various physical scales and space (or time) (Feng, 2011; Lei et al. 2018).

Band-pass filter

When the interference signal and effective signal are in different frequency ranges, the interference signal can be suppressed by the band-pass filter. By identifying the frequency range of the effective signal, the amplitude of the signal within this frequency band remains unchanged, and the amplitude outside the frequency band is set to 0.

Short-time Fourier transform

We performed a joint time–frequency domain transform of the seismic signal using STFT based on the pre-analyzed data. This process allows both the time domain distribution and frequency domain information of the seismic signal to be obtained (Yan et al.

2017, 2019). The idea behind STFT is outlined briefly here. Equation 1 shows the transform equation, $x[n]$ is a discrete time series, and $\omega[n]$ is a time–frequency localized window function. The analysis window function $\omega[n]$ is assumed stationary over a relatively short period (Yan et al. 2017).

$$\text{STFT}\{x(n)\}(m, \omega) \equiv X(m, \omega) = \sum_{n=-\infty}^{\infty} x[n]\omega[n-m]e^{-j\omega n} \quad (1)$$

For the STFT process, selecting a window function (Eq. 2) which is the Hanning window with a length of 128 points (Yan et al. 2017).

$$\omega[n] = \begin{cases} 0.5 - 0.5\cos\left(\frac{2\pi n}{N-1}\right), & (0 \leq n \leq N-1) \\ 0, & (\text{others}) \end{cases} \quad (2)$$

Power spectral density

The power of each frequency unit for each frequency band component corresponding to a specific moment can be estimated on the basis of the PSD of the seismic signal in the frequency domain (Yan et al. 2017). Tsai (2012) proposed a seismic signal PSD estimation model for sediment transport (Eq. 3).

$$P(f, D) \approx \frac{n}{t_i} \frac{\pi^2 f^3 V_p^2 w_i^2}{v_c^2 v_u^2} \chi(\beta) \quad (3)$$

where v_c is the Rayleigh-wave phase velocity, v_u is the group velocity at 1 Hz, V_p is the boulder volume, n is the number of boulders in the group, $\frac{n}{t_i}$ is the sediment flux, and $\chi(\beta) \equiv \int_{-\infty}^{\infty} \frac{1}{\sqrt{1+y^2}} e^{-\beta\sqrt{1+y^2}} dy$.

Lai et al. (2018) proposed a PSD estimation model for debris flow seismic signals based on the PSD model of fluvially flows by Tsai (2012) and simplified it:

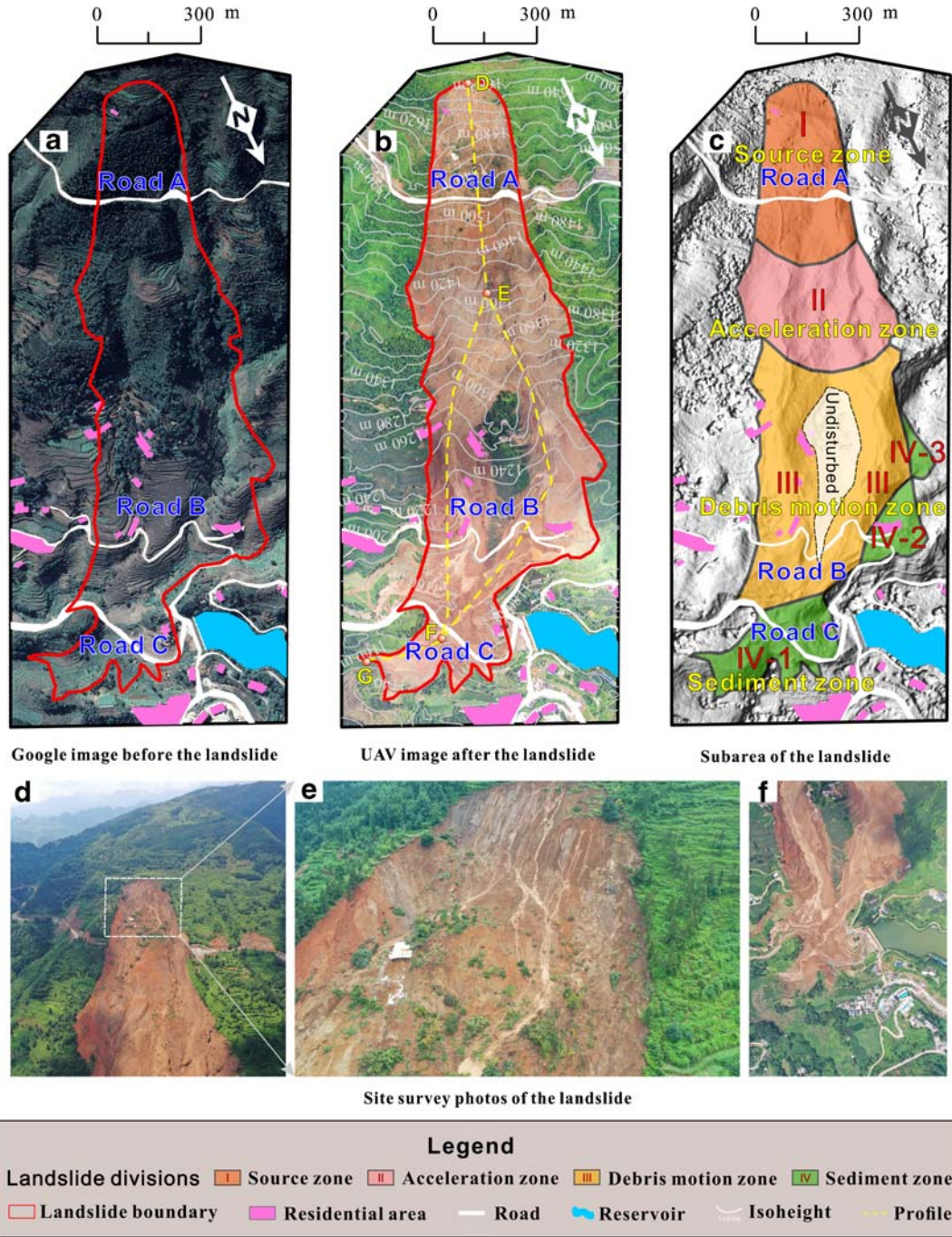


Fig. 4 Comparison of remote sensing images taken before and after the Shuicheng landslide. **a** Before the landslide. **b** Aerial image after landslide. **c** Landslide survey profile. **d–f** Landslide site survey photos. **d** Upper part of the landslide area. **e** Sedimentary area in the upper part of the landslide (enlarged area marked by white rectangle in Fig. 4d), showing a relatively intact roof of a house at the top of the landslide. **f** Sediment characteristics at the bottom of the landslide area

$$P(f, D) \approx 1.9 \cdot LWD^3 u^3 \cdot \frac{f^{3+5\xi}}{v_c^2 r_0} e^{-\frac{8.8 f^{1+\xi} r_0}{v_c Q}} \quad (4)$$

where $\xi \approx 0.25-0.5$ is a parameter related to how strongly the seismic velocities increase with depth at the site (Tsai et al. 2012), D is per unit grain size, v_c is the Rayleigh-wave phase velocity, r_0 is

the average distance of the station from the debris slide, Q is the quality factor for the Rayleigh waves (assumed independent of frequency within the observed range), and P is the seismic PSD of the velocity as a function of f and has units of $(\text{m/s})^2/\text{Hz}$. u is the velocity of the flow, L is the length of the debris end of the landslide mass, and W is the channel width.

The PSD of a seismic signal in the frequency domain can be expressed as Eq. 5, which is used to analyze the statistical

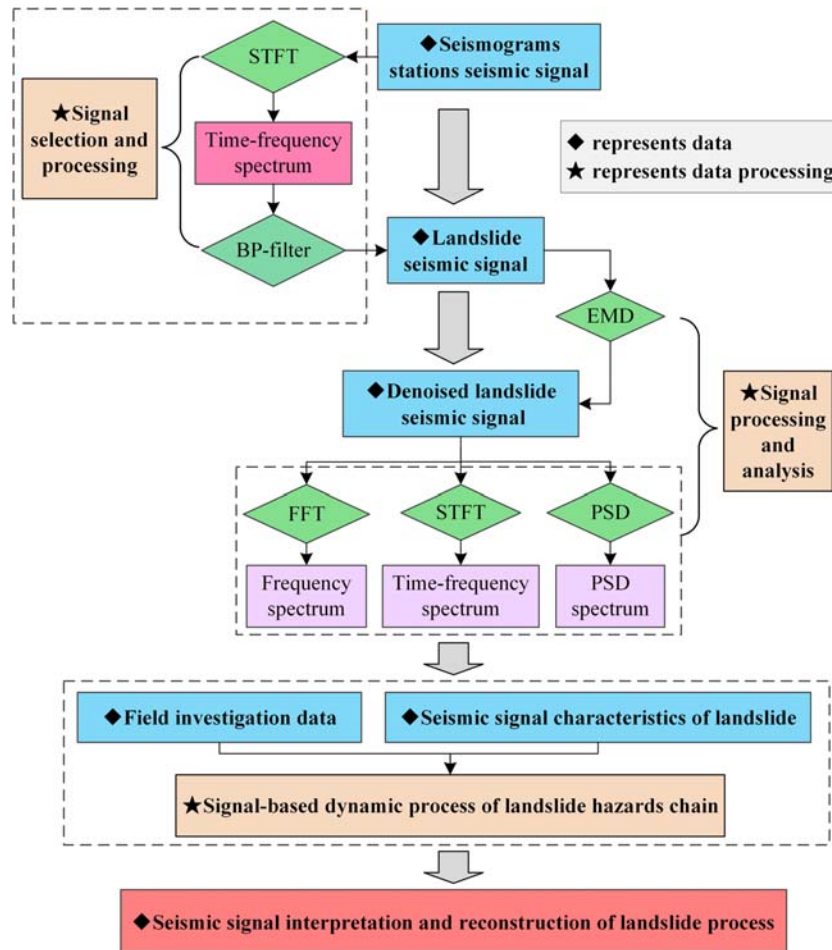


Fig. 5 Seismic signal analysis and processing flow chart

characteristics of each component of the landslide seismic signal and its source (Yan et al.2017).

$$PSD_{f_{\min} \sim f_{\max}}(t) = \frac{1}{(f_{\max} - f_{\min})} \times \sum_{f=f_{\min}}^{f_{\max}} S(t, f) \Delta f \quad (5)$$

Where f_{\min} and f_{\max} represent the lowest and highest frequencies in the band to be analyzed, respectively, t represents time, and $S(t, f)$ represents the time-frequency power spectrum of the seismic signal calculated using STFT.

In the actual application of PSD, we often use Eq. 6 to calculate the PSD of the seismic signal, whose PSD is the accumulation of all particle sizes and all frequencies, and this represents the integral of the PSD amplitude generated for all granularities. We have to integrate the PSD models (Eqs. 3 and 4) along f and D (Eq. 5), which is the PSD energy of all frequencies and sizes at a single moment.

$$PSD(t) = \iint PdDdf \quad (6)$$

Results and discussion

Signal selection and preliminary analysis

We extracted seismic data starting from 2 days before the landslide and conducted preliminary analysis. Clear identification of the

seismic signal of the landslide from the data of each seismic station was difficult. The signals of the 14 stations can be divided into two categories. The first type of signal exhibits environmental noise characteristics and the seismic characteristics related to landslides cannot be identified from the original records. There is no clear time spectrum pattern and the frequency range is not uniform (Fig. 6a, b, c). There are 12 main stations with this type of signal. The second type of signal shows spindle-shaped characteristics of the landslide signal over the time-frequency spectrum. There are “peak-like” or single peaks over the frequency range of 0–45 Hz. Of the 14 stations, only stations QIJ and GYA contain such signals (Fig. 6d, e).

According to statistics of landslide and debris flow seismic signals from previous studies, the frequency of landslide seismic signal is generally lower than 20 Hz (Table 1). Generally, larger landslide volumes and shorter landslide durations are associated with wider signal frequency bands. The volume of the landslide was about $200 \times 10^4 \text{ m}^3$. Station GYA with a straight-line distance of 222 km and station QIJ with a distance of 168 km can receive high-frequency information up to 45 and 20 Hz, respectively. The effective frequency ranges show large differences compared with the statistical features reported in the literature. In addition, the signal start time at QIJ is about 3 min later than the actual time at GYA. The bandwidth of the QIJ signal is about half of the frequency range of the GYA signal. Stations GYA and QIJ are located NEE and NW of the landslide, but the geological features of the areas

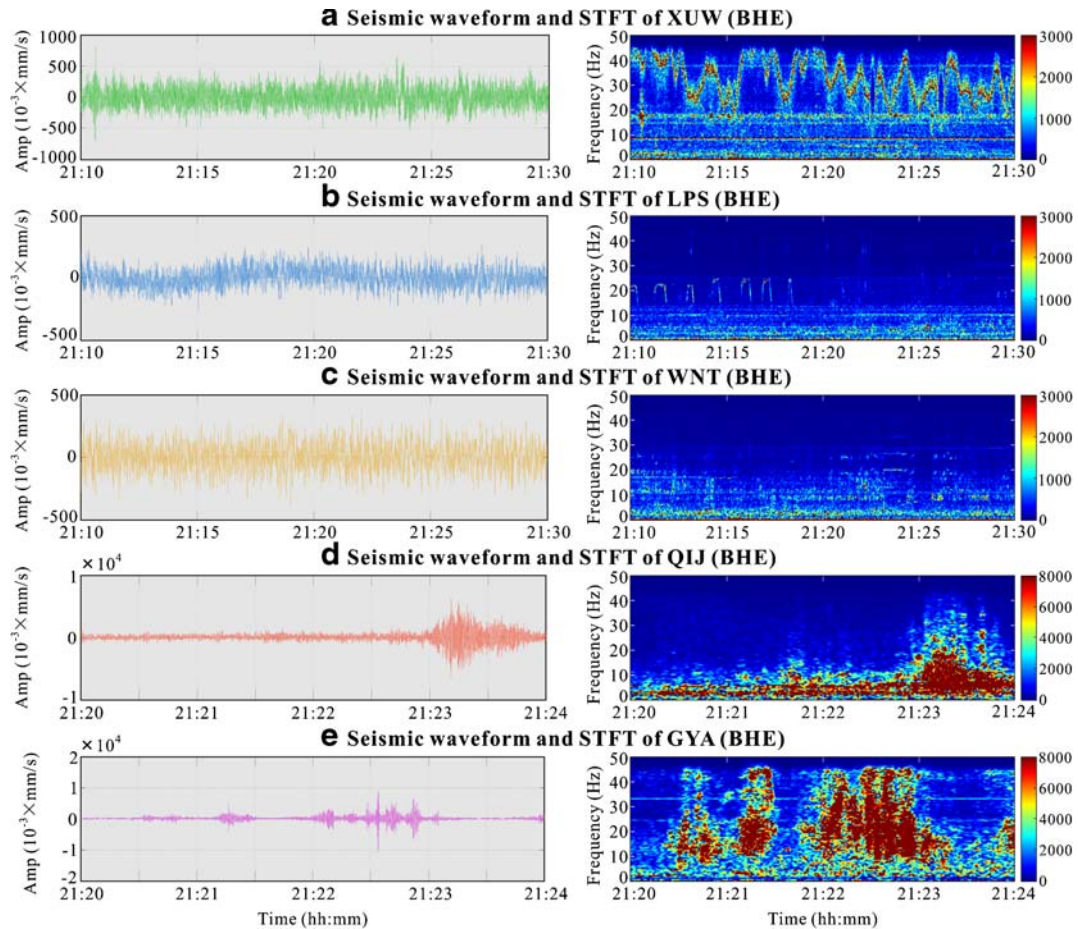


Fig. 6 Time domain seismic curves and STFT-spectrum of five typical stations in this study. a–e Seismic signals before and after the landslides recorded by stations XUW, LPS, WNT, QIJ, and GYA and their time–frequency spectrum, respectively

are similar and the differences in surface features are not sufficient to cause such a large difference between the starting times and frequency ranges. The seismic signals recorded at GYA and QIJ reflect the duration of a single landslide event (“spindle”) of about 1.5 min, which is inconsistent with the eyewitness evidence that the landslide duration was about 5 min. Furthermore, the stations closer to the landslide site did not record similar features to those of stations GYA and QIJ. We therefore conclude that the seismic signals recorded by the QIJ and GYA stations are not related to this landslide.

Among the 14 stations, XUW is closest to the landslide site and received the strongest signal of all the stations. The time spectrum of the original seismic signal of XUW has a relatively continuous energy level between 0 and 10 Hz but no continuity in the spectral band of 10–20 Hz. Between 20 and 50 Hz, the spectral energy fluctuates as shown in Fig. 6a. On the basis of these time–frequency characteristics, three band-pass filters of 0–10, 10–20, and 20–50 Hz were designed and the time domain seismic curves and time–frequency spectra of these three frequency bands were obtained. The time–frequency spectra of these three intervals all show irregular noise characteristics (Fig. 7a, b, c) and the spectrum of the 0–10 Hz band is weakened at 5 Hz. However, strong low-frequency energy (less than 1 Hz) appears throughout the time

history (Fig. 7a). To further highlight the continuous energy band around 5 Hz, the signal was passed through a band-pass filter of 4.5–6 Hz (Fig. 7d). The seismic curve of this frequency range shows more clear spindle-shaped characteristics, which is typical of landslide seismic signals. The continuous energy band around 5 Hz in the time spectrum is strengthened, which is more in line with the statistical characteristics of landslide signals (Table 1).

The seismic curve and time spectrum in Fig. 7d show higher noise levels. To enhance the effective signal and attenuate the noise, the seismic data in the 4.5–6 Hz frequency range was subjected to EMD processing. As shown in Fig. 8, the energy of the intrinsic mode function 1 (IMF1) occupies 99.1% of the original energy, which has a similar spectrum to the undecomposed signal. IMF2–IMF5 exhibit noise characteristics and each IMF component exhibits low-frequency characteristics. For this analysis, we use IMF1 as the landslide signal recorded at station XUW. As shown in Fig. 9, the noise of IMF1 is significantly attenuated and the time spectrum is cleaner.

In the same manner, we obtained the seismic curves of the main IMF components of the other 11 stations in the range of 0–10 Hz. Comparative analysis shows that except for the weak amplitude recorded at station LPS and the strong amplitude at XUW, the records of the other stations show background noise and no obvious regularity in the time spectrum. Station LPS recorded

Table 1 Statistics of seismic signal parameters of landslide events

Event/year	Duration (s)	Frequency Range/Hz	Time domain feature	Time–frequency feature	Landslide volume/10 ⁴ m ³	Reference
Tavanasa collapse/2002	40	1–10	Single spindle	Single peak	9	Dammeier et al. 2011
Laguna Beach landslide/2005	35	0–4	Double spindle	Double peak	44.5	Richter and Trigg 2008
Aiguille Dru collapse/2005	50	1–8	Double spindle	Double peak	15	Dammeier et al. 2015
Monte Rosa collapse/2007	110	1–18	Single spindle	Single peak	30	Huggel 2009
Formazza collapse/2009	100	1–25	Single spindle	Single peak	70	Dammeier et al. 2015
Shiaolin landslide/2009	80	0–3	Single spindle	Single peak	2500	Tsou et al. 2011
Akatani landslide/2011	85	0–0.5	Single spindle	Single peak	8200	Yamada et al. 2013
Preonzo collapse/2012	80	1–20	Single spindle	Single peak	21	Loew et al. 2017
Xinmo landslide/2017	100	0–2	Double spindle	Double peak	1882	Wen et al. 2017
Piz Cengalo collapse/2017	130	1–20	Single spindle	Single peak	315	Amann et al. 2018

the seismic signal only at the fastest stage of the landslide debris movement, while the seismic signal at other stages is attenuated by strong absorption during the propagation process, which is difficult to separate from the background noise. Therefore, in this study, only seismic data of from station XUW are used to reconstruct the landslide process.

Seismic signal characteristics of the landslide

The seismic intensity of the Shuicheng landslide signal recorded at station XUW of the China Earthquake Administration is relatively low in the N, E, and Z directions (Fig. 9), showing a low SNR and the most severe SNR (effective signal amplitude/noise). The amplitude is about 2, which indicates that the scale of the landslide is relatively small.

The seismic curve shows two abnormal amplitudes at 21:18:45 and 21:20, which may correspond to the starting time of the landslide. In the time spectrum, a distinct band of higher energy is seen in the E and N components at 21:20 while the Z-component energy band is relatively weak. The E-component has a slightly wider frequency range, slightly stronger energy, and a lower frequency. At about 4.5–5.5 Hz, the frequency of the N component is slightly higher, the energy is slightly weaker, and the frequency range is slightly narrower (~ 4.8–5.7 Hz). The Z-component has the lowest frequency, weakest energy, and narrowest frequency range. The time spectrum of the three components at station XUW is at 21:25:10 where there is a downwardly inclined monoclinic energy cluster. At this moment, the seismic amplitude of the three components in the time domain seismic curve decreases. The energy level of the ambient noise is small and both the N and Z components appear as vertices of a small “inverted triangle.” According to the site investigation, the landslide began at about 21:20 and lasted 3–4 min. This information, combined with the time–

frequency characteristics of the seismic curve, indicates that the start time of this landslide was 21:20, the termination time was 21:25:10, and the landslide duration was 4 min and 10 s.

According to the time and frequency domain characteristics, the landslide seismic curve can be divided into four segments or phases (Fig. 9). The characteristics of the E, N, and Z components of the seismic signal in the first stage are slightly stronger than the noise level. The second, third, and fourth stages show clear abnormalities with respect to the noise, which may correspond to the main process of the landslide.

The second to fourth stages constitute the main stage of the signal. The spindle-shaped characteristics of the three components in the time domain differ. The seismic curve in the E direction shows a box shape that evolves into a spindle feature. The seismic curve in the N direction exhibits an inverted triangle characteristic, followed by a spindle shape with a relatively low amplitude. The Z direction also exhibits a seismic characteristic similar to noise in the second phase but its energy is slightly stronger than the background noise. Between the end of the second to the end of the fourth stage, the seismic curve in the Z direction generally exhibits an elongated spindle shape.

In the time–frequency domain, the energy peaks of the spectrum in the three directions form an inverted “W” shape. That is, as the landslide progressed, the frequency of the seismic signal decreased, increased, decreased, and then increased again. The E and N components of the time–frequency spectra have high energy in the second and third phases within the frequency range of 5.1 and 6 Hz. The peak energy shifts from 6 to 5.1 Hz and then up to 5.7 Hz. The Z component is weaker in the second phase with only sporadic energy clusters, and high energy clusters mainly appear in the third phase. In the fourth phase, the energy in all three directions is weak, but the frequency is relatively high, within 5.25–6 Hz.

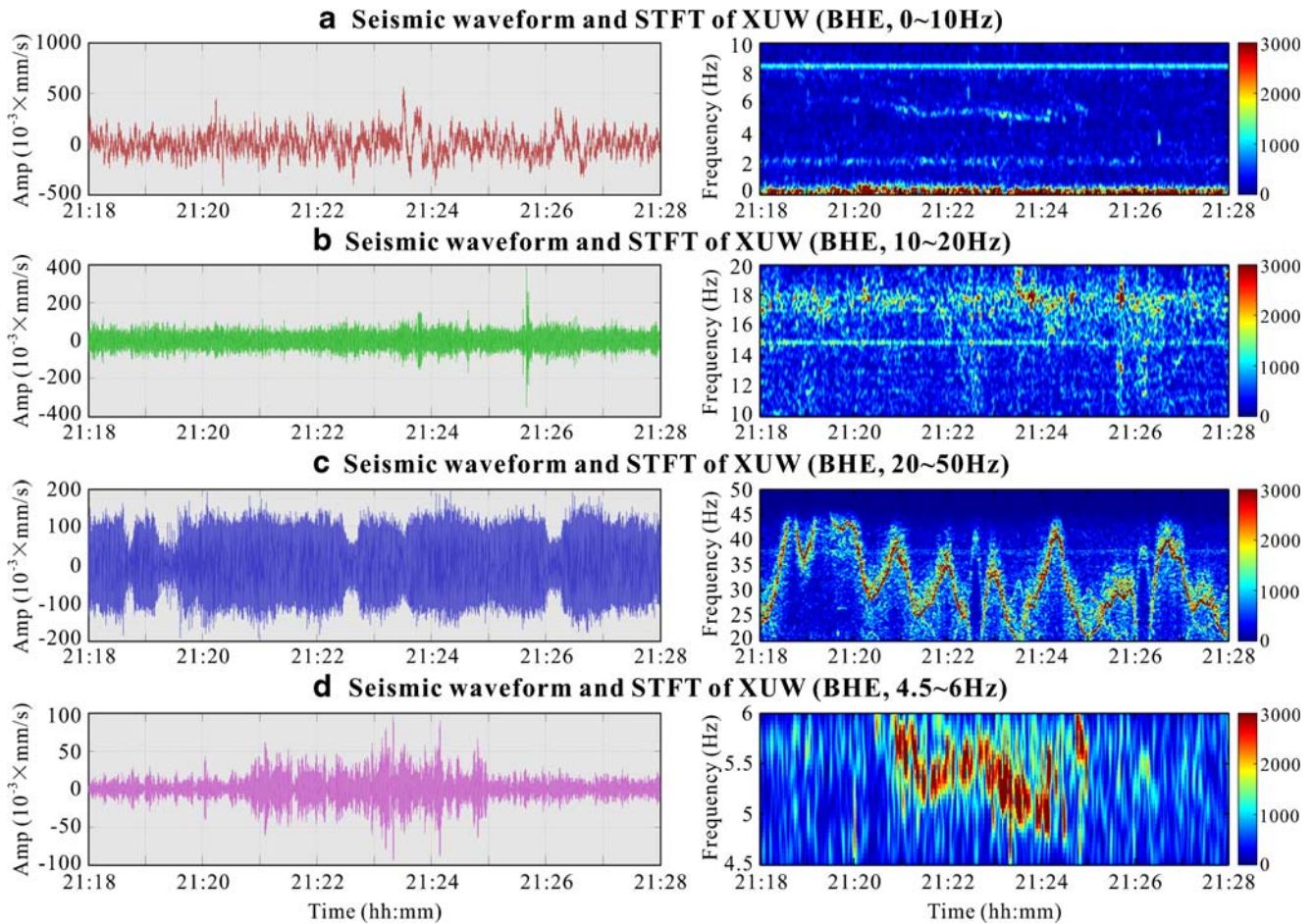


Fig. 7 Time domain seismic curves and STFT-spectra of station XUW data in four frequency bands

The PSD parameter changes, which reflect the particle size, velocity, and number of particles in the landslide debris, can also be divided into four stages as in the time domain curve and time-frequency spectrum (Fig. 10). In the first stage, all three components start with a single pulse, and the PSD energy then rapidly decreases to a level slightly higher than the background noise but still tends to gradually increase in energy with varying gradients. In the second stage, the energy in the E and N directions rapidly increases and then begins to oscillate. The Z direction is similar to the first stage: the energy begins at the noise level but slowly rises. In the third stage, the energy curves in the three directions have a peak but the E direction has an additional peak at the end. In the fourth stage, the energy curves of the three directions all show a downward trend towards a trough, then rise to a high-energy peak, which is most prominent in the E direction, while those in the N and Z directions are of lower energy.

Signal-based dynamic processing of landslide hazard chain

Based on the combined analysis of the precipitation in Shuicheng County, geological and topographic conditions, geological survey of the landslide site, and the seismic signal characteristics recorded at station XUW, the landslide evolution can be divided into four stages: the fracture-transition stage; accelerated initiation stage; bifurcation-scraping stage; and deposition stage. These four stages are the same as the four stages reflected by the seismic signal.

1) Fracture-transition stage

This phase corresponds to the signal characteristics of the first phase, starting with a strong sharp pulse, which corresponds to a collapse event. The PSD energy after the sharp pulse increases slowly, corresponding to slow landslide phenomena. Road A absorbs the surface water, which gradually increases the water saturation of the weathered rock mass (surface soil) on the lower side of the road. On the upper side of the road, the surface soil gradually liquefies and the friction between the soil gradually decreases. When the surface soil liquefies, the accumulated water continuously penetrates downward, which gradually increases the soil liquefaction in the deeper parts and causes the coupling force between the soil and bedrock to gradually weaken, enabling easier sliding. The increase in water saturation also increases the gravitational force of the soil on the slope. The combination of the three processes causes a vulnerable part of the slope to begin to collapse downward, generating the initial seismic signal, which corresponds to the energy spectral peak over a wide frequency band at 21:20 in the time-frequency spectrum (Fig. 9).

At this stage, the sliding part has a relatively small volume and cannot directly trigger a large-scale landslide. However, the collapse reduces the stability in the entire area. This instability causes extensive small-scale continuous sliding that is not

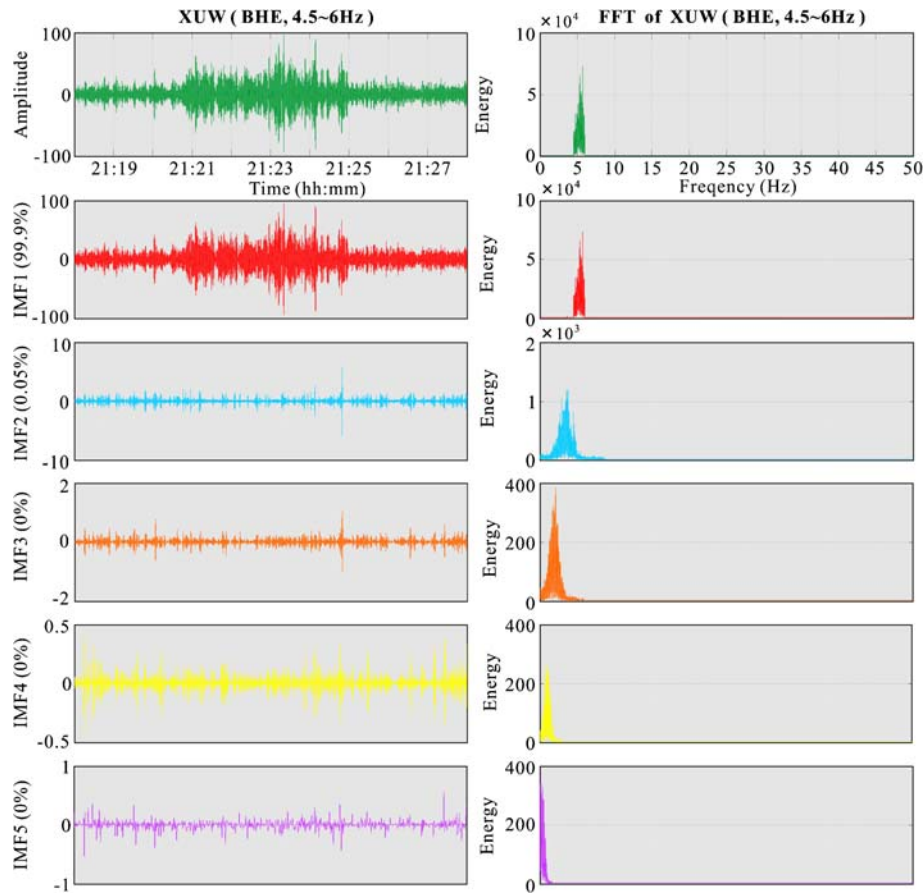


Fig. 8 EMD decomposition result of the 4.5–6 Hz band seismic signal and spectrum of the corresponding IMF component from station XUW

detectable by the seismic station. These small-scale slips allow higher-weathered layers to accumulate on the underlying soil, which most likely accumulate on the gentle platform below Road A and on the gentle slope below the platform (Fig. 11a). The accumulation of the landslide body changes the original balance below and the landslide mass gradually begins to slide. The upper part slides down so that the weathered layer of the sliding source area loses the support of the lower part and also gradually begins to slide downward. This sliding is relatively slow overall, which can be confirmed from the thicker accumulation area in the sliding source area and the roof that completely retains the house at the top of the landslide. However, as the landslide progresses, the overall sliding speed gradually increases, and the PSD curve shows a tendency to slowly increase in all three directions.

2) Accelerated initiation stage

This phase corresponds to the second phase of the seismic signal; the main feature of which is opposite characteristics observed in the E, N, and Z direction curves. The E and N direction time domain amplitude values are large, the time-frequency domain energy cluster is strong, the frequency is high, and the PSD exhibits high energy characteristics, while the Z direction amplitude is slightly higher than the background noise and only the weaker high-frequency energy is

observed in the time spectrum. The mass and PSD curves are slightly higher than the noise level (Figs. 9 and 10), indicating that the main direction of motion of the landslide body is horizontal and along the relatively gentle slope.

At this stage, the weathered layer accumulated on the wide platform and the periphery of the platform gradually destabilizes under the action of the landslide deposits, and the movement is gentler along the lower part of the platform. The weathered layer, which slowly slides down during the fracture-transition phase, accumulates on the steeper slope of the road (i.e., below the road, at the rear of the gentle platform), forming a new gentle slope that continuously grows (Fig. 11b). In the process, its stability gradually weakens and at some point it loses its balance and moves downward at a higher speed. Owing to the gentle platform and gentle slope below it, the displacement of the landslide body during this movement is mainly in the horizontal direction. The longitudinal motion (in the Z direction) is relatively small and the movement speed has the same characteristics.

Two valleys develop on both sides of the wide platform to form a natural debris transport channel. During this process, the landslide body gradually merges into the two valleys and its movement speed gradually increases as well as the longitudinal velocity component, which is indicative of entering the most destructive stage of the landslide: the bifurcation-scraping stage (Fig. 11c).

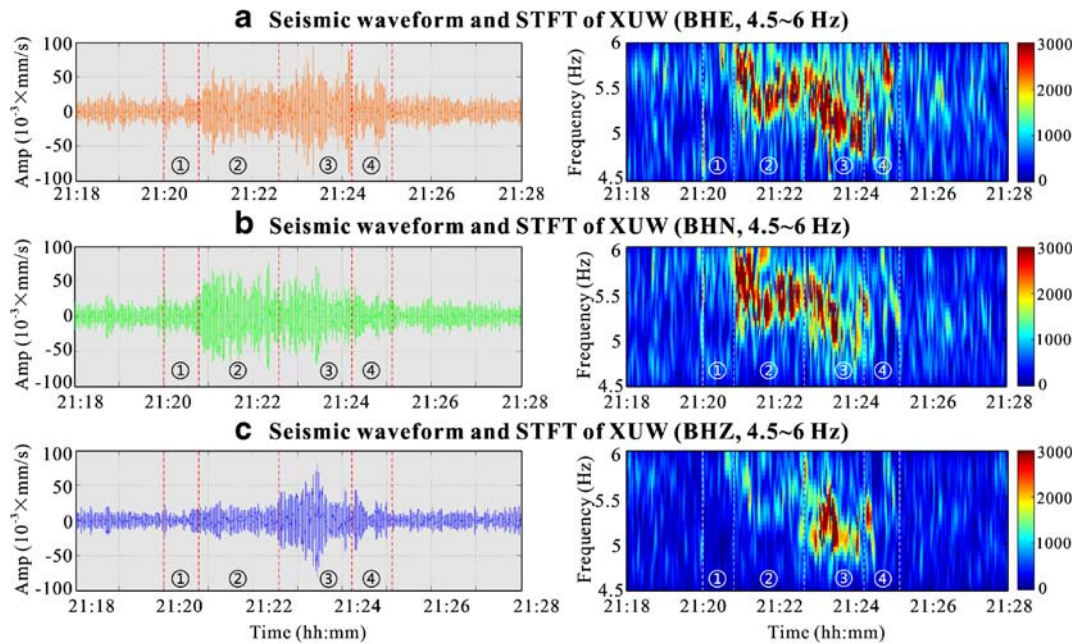


Fig. 9 Time domain signals and STFT-spectrum of the E, N, and Z components of the landslide seismic signal recorded at station XUW. Four stages can be easily distinguished along the time domain signals and time–frequency spectra: ① low-energy state and the beginning of the high-amplitude stage; ②–④ relatively high-energy stages, the time–frequency spectrum of the three stages is W-shaped, which may correspond to the high-energy stage of the landslide. The amplitudes and time–frequency spectrum of stages ②, ③, and ④ in the three directions reflect different characteristics, corresponding to the different landslide elements at the different stages

3) Bifurcation-scraping stage

This phase corresponds to the third phase of the seismic data, in which the three components exhibit the same characteristics in the time domain, time–frequency energy spectrum, and PSD curves. The PSD energy in all three directions reaches the maximum value at this stage, especially the Z direction signal, where the amplitude of the time domain, the frequency range of the time–frequency spectrum, the energy, and the PSD amplitude values are higher than in the other stages.

The landslide at this stage is divided into two sections and moves along the valley (Fig. 11c). After the landslide body accelerates, the east and west sides of the platform merge into the east and west valley, respectively. The upper part of the valley on the east and west side (below the platform) has a large slope, and the landslide body moves in the horizontal direction after entering the valley. The movement is dominated by vertical motion and the speed rapidly increases. The slope of the valley gradually broadens near Road B and the landslide body collides with the nearby wide valley with high energy and fast longitudinal speed. The grounding is reduced and the collision moment reflects the maximum speed of the landslide body, which corresponds to the spike of the third phase on the PSD curve in all three directions.

After the impact, the landslide body in the valley on the east side continues to move downward with greater kinetic energy, which smothers the vegetation and houses on both sides of the valley. The landslide at this stage causes the largest human and economic loss.

The valley on the west side is relatively deeper and steeper and the central direction of the valley changes. This part has a more obvious “cross-shore sedimentation”, that is, at the turn of the valley, the landslide body rushes towards the west slope of the valley with greater kinetic energy. Part of the landslide debris crosses the west slope. After crossing the shore, owing to the loss of the channel constraint, the velocity rapidly decreases and deposition occurs, forming two debris deposits on the valley slope (IV-2, IV-3 of Fig. 4c). The “over the shore” that occurs when the valley is changing may correspond to the second small pulse of the PSD curve in the third stage.

4) Deposition stage

In the vicinity of Road C, the restraining effect of the valley on the landslide body gradually weakens and the lateral movement of the landslide body gradually strengthens. Especially at the mouth of the west and east valleys, the lateral movement causes the two landslide masses from the east and west valleys to converge into one body. The whole landslide body is then deposited at the bottom of the gorge, resulting in a large accumulation of landslide mass and debris. Large slope deposits were laid in the sedimentary areas below the two valleys and Road C (Fig. 11d). The lateral migration caused the lateral velocity to rapidly increase; thus, the small increase in the frequency, amplitude, and PSD of the E-component corresponds to the sharp pulse of the E-component seismic record during the onset of the fourth phase. At this stage, the components of the landslide velocity in all three directions

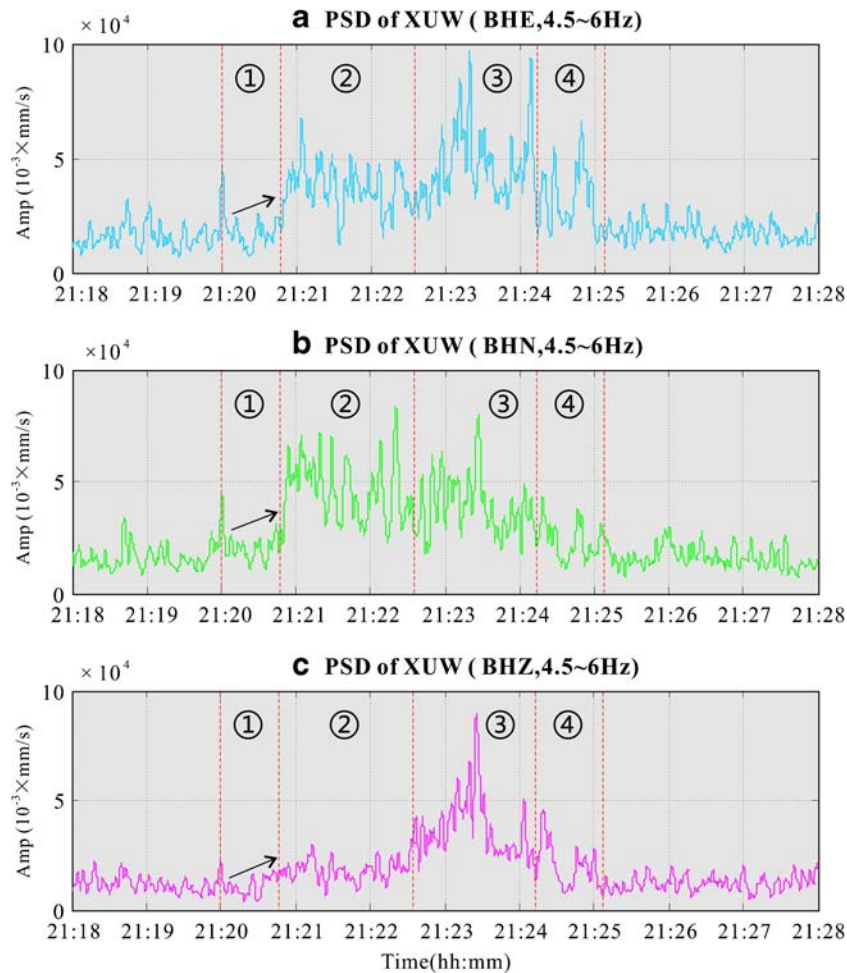


Fig. 10 Seismic PSD curves of the Shuicheng landslide recorded at station XUW, showing the various stages of the landslide progress. ① Starting stage; ② horizontal high energy and low vertical energy; ③ the unimodal PSD curve corresponds to the maximum value of landslide energy; ④ deposition stage—the decreasing PSD energy curve corresponds to the decrease in landslide energy

weaken rapidly, and the time domain seismic characteristics, time-frequency spectrum characteristics, and PSD energy curves in the three directions are all weakened. Similar to a river delta front, the main deposits are fine-grained sandy particles. The small and medium-sized debris of this landslide may move further down the valley in the future (Fig. 4c).

Conclusions and discussion

This study investigates the characteristics of seismic signals caused by the “7.23” Shuicheng landslide by using EMD, BP-filter, FFT, STFT, and PSD analyses. Combined with field investigation results, the following conclusions were drawn.

1. Our analysis indicates that the Shuicheng landslide is a surface weathering shell landslide caused by rainfall. The landslide body is 415 m long and 207 m wide, with an area of about $8.6 \times 10^4 \text{ m}^2$, an average sliding depth of about 20 m, and a volume of about $1.72 \times 10^6 \text{ m}^3$.
2. Based on the characteristics of a weak landslide seismic signal and low SNR, a set of processes for separating the landslide seismic signal from the signal with low SNR is developed.

Among the 14 seismic stations near the landslide site, only station XUW clearly captured the entire landslide process. The seismic signal has weak energy and low frequency. The three components of the seismic curve in the time domain exhibit spindle-shaped features and the energy spectra of the time-frequency plots of the three components exhibit a “W” shape which differs between the components.

3. The landslide process can be divided into four stages: the fracture-transition stage; accelerated initiation stage; bifurcation-scraping stage; and deposition stage. The landslide has a distinct feature that the initial fracture point of the fracture-transition stage is not the slip source of the landslide. The area is located in the upper part of the landslide surface, that is, the slope part near Road A begins to slide first. The main body of the landslide is the middle and upper part of the landslide surface.
4. The seismic interpretations in this case study are useful for calibrating numerical simulations for future analysis of the dynamic behavior of the Shuicheng landslide. The signal processing methodology developed in this study provides theoretical guidance for a quick way to characterize and reconstruct a landslide process.

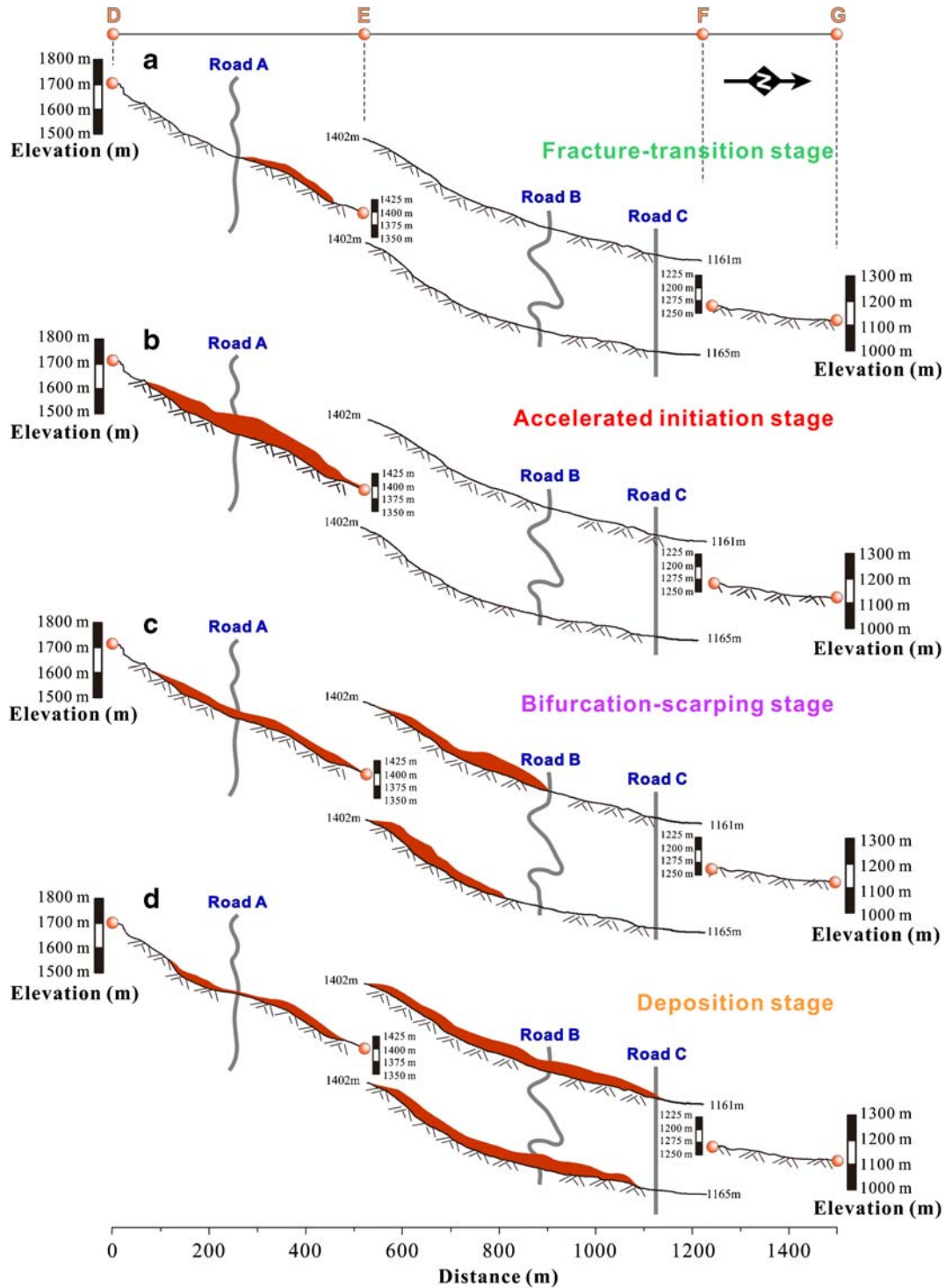


Fig. 11 Schematic diagram of the slopewash at the beginning of the four stages of the landslide process

The limitations of the current study are as follows: station LPS, which is 67 km from the Shuicheng landslide, only recorded the signal of the strongest stage, and the signal was transformed so strongly that the data of this station could not be applied to the landslide analysis. This makes the weak signal identification method proposed by the current study only applicable to a single station, and we could not use the analysis results of other stations to further verify the identified signals. If landslide data from

another seismic station located about 20 km from the landslide were available for analysis, we would be able to test the rationality of our analysis method and verify whether the XUW landslide signal was indeed generated by the landslide. However, due to cost limitations, the China Earthquake Administration cannot deploy seismic stations at such high density. Therefore, future work needs to establish a scientific evaluation system after studying multiple landslide cases.

The principal seismic direction of the landslide process can be obtained through the analysis of the three different components of a single station. For example, in the 2017 Xinmo landslide study, Bai et al. (2019), based on the joint analysis of multiple stations, determined more definitely the principal seismic direction. At the same time, by analyzing the wavelength properties of multiple stations such as frequency, waveform, and energy, we can clearly obtain the absorption and attenuation characteristics of the landslide's seismic signal during its propagation in the earth's crust (Feng, 2011). These characteristics also help to further verify the accuracy of the seismic signals we obtained. Relate the seismic signals to soil properties such as particle size distribution (Guo and Cui 2020; Shi et al. 2020) are also recommended in future research.

Acknowledgments

We acknowledge the Institute of Geophysics, China Earthquake Administration, for providing the seismic signal data recorded near the Shuicheng landslide. We thank Esther Posner, PhD, from Liwen Bianji, Edanz Editing China, for editing the English text of a draft of this manuscript.

Funding information This study was financially supported by the International Science & Technology Cooperation Program of China (grant no. 2018YFE0100100), National Natural Science Foundation of China (grant no. 41901008), National Key R&D Program of China (grant no. 2018YFC1505201), Open Fund Project of the Key Laboratory of Mountain Hazards and Surface Processes of the Chinese Academy of Sciences, and the Fundamental Research Funds for the Central Universities (grant no. 2682018CX05). This work was also financially supported by the China Scholarship Council.

References

Aleotti P, Chowdhury R (1999) Landslide hazard assessment: summary review and new perspectives. *Bull Eng Geol Environ* 58(1):21–44. <https://doi.org/10.1007/s100640050066>

Allstadt K (2013) Extracting source characteristics and dynamics of the August 2010 Mount Meager landslide from broadband seismograms. *Journal of Geophysical Research-Earth Surface* 118(3):1472–1490. <https://doi.org/10.1002/jgrf.20110>

Amann F, Kos A, Phillips M, Kenner R (2018) The Piz Cengalo Bergsturz and subsequent debris flows. *EGU General Assembly Conference Abstracts* 20:14700

Bai X, Jian J, He SM, Liu W (2019) Dynamic process of the massive Xinmo landslide, Sichuan (China), from joint seismic signal and morphodynamic analysis. *Bull Eng Geol Environ* 78(5):3269–3279. <https://doi.org/10.1007/s10064-018-1360-0>

Brodsky EE, Gordeev E, Kanamori H (2003) Landslide basal friction as measured by seismic waves. *Geophys Res Lett* 30(24):285–295. <https://doi.org/10.1029/2003GL018485>

Chen CH, Chao WA, Wu YM, Zhao L, Chen YG, Ho WY, Lin TL, Kuo KH, Chang JM (2013) A seismological study of landquakes using a real-time broad-band seismic network. *Geophys J Int* 194(2):885–898. <https://doi.org/10.1093/gji/ggt121>

Cui P, Zhu YY, Han YS, Chen XQ, Zhuang JQ (2009) The 12 May Wenchuan earthquake-induced landslide lakes: distribution and preliminary risk evaluation. *Landslides* 6(3):209–223. <https://doi.org/10.1007/s10346-009-0160-9>

Cui YF, Zhou XJ, Guo CX (2017) Experimental study on the moving characteristics of fine grains in wide grading unconsolidated soil under heavy rainfall. *J Mt Sci* 14(3):417–431. <https://doi.org/10.1007/s11629-016-4303-x>

Cui Y, Cheng D, Choi CE, Jin W, Lei Y, Kargel JS (2019) The cost of rapid and haphazard urbanization: lessons learned from the Freetown landslide disaster. *Landslides* 16(6):1167–1176. <https://doi.org/10.1007/s10346-019-01167-x>

Dammeier F, Moore JR, Haslinger F, Loew S (2011) Characterization of alpine rockslides using statistical analysis of seismic signals. *J Geophys Res* 127(3–4):166–178. <https://doi.org/10.1029/2011JF002037>

Dammeier F, Guilhem A, Moore JR, Haslinger F, Loew S (2015) Moment tensor analysis of rockslide seismic signals. *Bull Seismol Soc Am* 105(6):3001–3014. <https://doi.org/10.1785/0120150094>

Dammeier F, Moore JR, Hammer C, Haslinger F, Loew S (2016) Automatic detection of alpine rockslides in continuous seismic data using hidden Markov models. *Journal of Geophysical Research-Earth Surface* 121(2):351–371. <https://doi.org/10.1029/2011JF002037>

Ekström G, Stark CP (2013) Simple scaling of catastrophic landslide dynamics. *Science* 339(6126):1416–1419. <https://doi.org/10.1002/2015JF003647>

Favreau P, Mangeney A, Lucas A, Crosta G, Bouchut F (2010) Numerical modeling of landquakes. *Geophys Res Lett* 37(15):L15305. <https://doi.org/10.1029/2010GL043512>

Feng Z (2011) The seismic signatures of the 2009 ShiaoLin landslide in Taiwan. *Natural Hazards and Earth System Science* 11(5):1559–1569. <https://doi.org/10.5194/nhess-11-1559-2011>

Feng ZY, Lo CM, Lin QF (2017) The characteristics of the seismic signals induced by landslides using a coupling of discrete element and finite difference methods. *Landslides* 14(2):661–674. <https://doi.org/10.1007/s10346-016-0714-6>

Fuchs F, Lenhardt W, Bokelmann G, Grp AAW (2018) Seismic detection of rockslides at regional scale: examples from the Eastern Alps and feasibility of kurtosis-based event location. *Earth Surface Dynamics* 6(4):955–970. <https://doi.org/10.5194/esurf-6-955-2018>

Guo C, Cui Y (2020) Pore structure characteristics of debris flow source material in the Wenchuan earthquake area. *Engineering Geology* 267:105499

Guinau M, Tapia M, Pérez-Guillén C, Suriñach E, Roig P, Khazaradze G, Torné M, Royán MJ, Echeverría A (2019) Remote sensing and seismic data integration for the characterization of a rock slide and an artificially triggered rock fall. *Eng Geol* 257:105113. <https://doi.org/10.1016/j.enggeo.2019.04.010>

Guo J, Yi SJ, Yin YZ, Cui YF, Qin MY, Li TL, Wang CY (2020) The effect of topography on landslide kinematics: a case study of the Jichang town landslide in Guizhou. *China Landslides* doi:1–15. <https://doi.org/10.1007/s10346-019-01339-9>

Helmstetter A, Garambois S (2010) Seismic monitoring of Sechillienne rockslide (French Alps): analysis of seismic signals and their correlation with rainfalls. *Journal of Geophysical Research-Earth Surface* 115(F3):03016. <https://doi.org/10.1029/2009JF001532>

Hibert C, Ekström G, Stark CP (2014) Dynamics of the Bingham Canyon Mine landslides from seismic signal analysis. *Geophys Res Lett* 41(13):4535–4541. <https://doi.org/10.1002/2014GL060592>

Hibert C, Ekström G, Stark CP (2017) The relationship between bulk-mass momentum and short-period seismic radiation in catastrophic landslides. *Journal of Geophysical Research: Earth Surface* 122(5):1201–1215. <https://doi.org/10.1002/2016JF004027>

Huang CJ, Yin HY, Chen CY, Yeh CH, Wang CL (2007) Ground vibrations produced by rock motions and debris flows. *Journal of Geophysical Research-Earth Surface* 112(F2):F02014h doi:<https://doi.org/10.1029/2005JF000437>

Huang XH, Yu D, Xu Q, Su JR (2018) Dynamic processes of the 24 June 2017 Xinmo landslide in Maoxian revealed by broadband seismic records. *Chin J Geophys* 61(10):4055–4062 (in Chinese)

Huggel C (2009) Recent extreme slope failures in glacial environments: effects of thermal perturbation. *Quat Sci Rev* 28(11–12):1119–1130. <https://doi.org/10.1016/j.quascirev.2008.06.007>

Hungu O, Leroueil S, Picarelli L (2014) The Varnes classification of landslide types, an update. *Landslides* 11(2):167–194. <https://doi.org/10.1007/s10346-013-0436-y>

Kao H, Kan CW, Chen RY, Chang CH, Rosenberger A, Shin TC, Leu PL, Kuo KW, Liang WT (2012) Locating, monitoring, and characterizing typhoon-induced landslides with real-time seismic signals. *Landslides* 9(4):557–563. <https://doi.org/10.1007/s10346-012-0322-z>

Kuo HL, Lin GW, Chen CW, Saito H, Lin CW, Chen H, Chao WA (2018) Evaluating critical rainfall conditions for large-scale landslides by detecting event times from seismic records. *Nat Hazards Earth Syst Sci* 18(11):2877–2891. <https://doi.org/10.5194/nhess-18-2877-2018>

Lai VH, Tsai VC, Lamb MP, Ulizio TP, Beer AR (2018) The seismic signature of debris flows: flow mechanics and early warning at Montecito, California. *Geophys Res Lett* 45:5528–5535. <https://doi.org/10.1029/2018GL077683>

Lei Y, Cui P, Zeng C, Guo YY (2018) An empirical mode decomposition-based signal process method for two-phase debris flow impact. *Landslides* 15:297–307. <https://doi.org/10.1007/s10346-017-0864-1>

Levy C, Mangeney A, Bonilla F, Hibert C, Calder ES, Smith PJ (2015) Friction weakening in granular flows deduced from seismic records at the Soufrière Hills Volcano, Montserrat. *Journal of Geophysical Research-Solid Earth* 120(11):7536–7557. <https://doi.org/10.1002/2015JB012151>

Li Q, Tian YF, Jiang WL, Xu C, Jiao QS, Qian HT (2019) Landslide emergency report of Chagou group, Pingdi village, Jichang town, Shuicheng County, Guizhou (V2.0). <http://www.eq-icd.cn/Index/show/catid/248/id/4653.html/> (in Chinese)

Li ZY, Huang XH, Xu Q, Yu D, Fan JY, Qiao XJ (2017) Dynamics of the Wulong landslide revealed by broadband seismic records. *Earth, Planets and Space* 69:27–10. <https://doi.org/10.1186/s40623-017-0610-x>

Lin CH (2015) Insight into landslide kinematics from a broadband seismic network. *Earth, planets and space* 67(1):8 doi:<https://doi.org/10.1186/s40623-014-0177-8>

Loew S, Gschwind S, Gischtig V, Keller-Signer A, Valenti GJL (2017) Monitoring and early warning of the 2012 Preonzo catastrophic rockslope failure. *Landslides* 14:141–154. <https://doi.org/10.1007/s10346-016-0701-y>

- Lombardo L, Bakka H, Tanyas H, Westen C, Mai PM, Huser R (2019) Geostatistical modeling to capture seismic-shaking patterns from earthquake-induced landslides. *Journal of Geophysical Research-Earth Surface* 124(7):1958–1980. <https://doi.org/10.1029/2019JF005056>
- Moore JR, Pankow KL, Ford SR, Koper KD, Hale JM, Aaron J, Larsen CF (2017) Dynamics of the Bingham Canyon rock avalanches (Utah, USA) resolved from topographic, seismic, and infrasound data. *Journal of Geophysical Research: Earth Surface* 122(3):615–640. <https://doi.org/10.1002/2016JF004036>
- Moretti L, Mangeney A, Capdeville Y, Stutzmann E, Huggel C, Schneider D, Bouchut F (2012) Numerical modeling of the Mount Steller landslide flow history and of the generated long period seismic waves. *Geophys Res Lett* 39(16):L16402. <https://doi.org/10.1029/2012GL052511>
- Ouyang C, An H, Zhou S, Wang Z, Su P, Wang D, Cheng D, She J (2019) Insights from the failure and dynamic characteristics of two sequential landslides at Baige village along the Jinsha River, China. *Landslides* 16 (7):1397-1414
- Ogiso M, Yomogida K (2015) Estimation of locations and migration of debris flows on Izu-Oshima Island, Japan, on 16 October 2013 by the distribution of high frequency seismic amplitudes. *J Volcanol Geotherm Res* 298:15–26. <https://doi.org/10.1016/j.jvolgeores.2015.03.015>
- Ouyang C, Zhao W, He S, Wang D, Zhou S, An H, Wang Z, Cheng D (2017) Numerical modeling and dynamic analysis of the 2017 Xinmo landslide in Maoxian County, China. *Journal of Mountain Science* 14 (9):1701-1711
- Petley DN (2013) Characterizing giant landslides. *Science* 339(6126):1395–1396. <https://doi.org/10.1126/science.1236165>
- Richter HH, Trigg KA (2008) Case history of the June 1, 2005 Bluebird Canyon landslide in Laguna Beach, California. *GeoCongress 2008: Geosustainability and Geohazard Mitigation*:433–440 doi:[https://doi.org/10.1061/40971\(310\)54](https://doi.org/10.1061/40971(310)54)
- Sakals ME, Geertsema M, Schwab JW, Ford VN (2012) The Todagin Creek landslide of October 3, 2006, Northwest British Columbia, Canada. *Landslides* 9(1):107–111. <https://doi.org/10.1007/s10346-011-0273-9>
- Schimmel A, Hübl J (2016) Automatic detection of debris flows and debris floods based on a combination of infrasound and seismic signals. *Landslides* 13(5):1181–1196. <https://doi.org/10.1007/s10346-015-0640-z>
- Schneider D, Bartelt P, Caplan-Auerbach J, Christen M, Huggel C, McArdell BW (2010) Insights into rock-ice avalanche dynamics by combined analysis of seismic recordings and a numerical avalanche model. *J Geophys Res* 115(F4). <https://doi.org/10.1029/2010JF001734>
- Sheng MH, Chu RS, Wei ZG, Bao F, Guo AZ (2018) Study of microseismicity caused by Xishancun landslide deformation in Li country, Sichuan Province. *Chin J Geophys* 61(01):171–182 (in Chinese)
- Shi XS, Nie J, Zhao J, Gao Y (2020) A homogenization equation for the small strain stiffness of gap-graded granular materials. *Computers and Geotechnics* 121:103440
- Si JF, Yin HF, Li FD, Zhang BJ, Li MY (2012) Characteristics and causes of geological hazards and the preventive measures in Shuicheng, Guizhou, China. *The Chinese Journal of Geological Hazard and Control* 23(1):111–115 (in Chinese)
- Tsai VC, Minchew B, Lamb MP, Ampuero JP (2012) A physical model for seismic noise generation from sediment transport in rivers. *Geophys Res Lett* 39(2):189–202. <https://doi.org/10.1029/2011GL050255>
- Tsou CY, Feng ZY, Chigira M (2011) Catastrophic landslide induced by typhoon Morakot, Shialin, Taiwan. *Geomorphology* 127(3–4):166–178. <https://doi.org/10.1016/j.geomorph.2010.12.013>
- Vilajosana I, Suriñach E, Abellán A, Khazaradze G, García D, Llosa J (2008) Rockfall induced seismic signals: case study in Montserrat, Catalonia. *Natural Hazards and Earth System Science* 8(4):805–812. <https://doi.org/10.5194/nhess-8-805-2008>
- Wen MS, Chen HQ, Zhang MZ, Chu HL, Wang WP, Zhang N, Huang Z (2017) Analysis of the characteristics and genetic mechanism of the 6.24 landslide in Maoxian County, Sichuan Province. *The Chinese Journal of Geological Hazard and Control* 28(03):1–7(in Chinese) doi:<https://doi.org/10.16031/j.cnki.issn.1003-8035.2017.03.01>
- Xu C, Qian HT, Jiang WL, Ren JJ, Ma SY, Li Q, Du Y (2019) Landslide emergency report of Chagou formation, Pingdi Village, Jichang Town, Shuicheng County, Guizhou. <http://www.eqjcd.cn/Index/show/catid/208/id/4649.html/> (in Chinese)
- Yamada M, Matsushi Y, Chigira M, Mori J (2012) Seismic recordings of landslides caused by typhoon Talas (2011), Japan. *Geophys Res Lett* 39(13):L13301. <https://doi.org/10.1029/2012GL052174>
- Yamada M, Kumagai H, Matsushi Y, Matsuzawa T (2013) Dynamic landslide processes revealed by broadband seismic records *Geophysical Research Letters* 40(12):2998–3002 <https://doi.org/10.1002/grl.50437>
- Yan Y, Cui P, Chen SC, Chen XQ, Chen HY, Chien YL (2017) Characteristics and interpretation of the seismic signal of a field-scale landslide dam failure experiment. *J Mt Sci* 14(2):219–236. <https://doi.org/10.1007/s11629-016-4103-3>
- Yan Y, Li T, Liu J, Wang WB, Su Q (2019) Monitoring and early warning method for a rockfall along railways based on vibration signal characteristics. *Sci Rep*, 2019, 9:6606 doi:<https://doi.org/10.1038/s41598-019-43146-1>
- Yesilnacar E, Topal T (2005) Landslide susceptibility mapping: a comparison of logistic regression and neural networks methods in a medium scale study, Hendek region (Turkey). *Eng Geol* 79(3–4):251–266. <https://doi.org/10.1016/j.enggeo.2005.02.002>
- Huang RQ (2009) Some catastrophic landslides since the twentieth century in the southwest of China. *Landslides* 6(1):69–81. <https://doi.org/10.1007/s10346-009-0142-y>
- Zhang Z, He SM, Liu W, Liang H, Yan SX, Deng Y, Bai XQ, Chen Z (2019) Source characteristics and dynamics of the October 2018 Baige landslide revealed by broadband seismograms. *Landslides* 16(4):777–785. <https://doi.org/10.1007/s10346-019-01145-3>
- Zhao J, Moretti L, Mangeney A, Stutzmann E, Kanamori H, Capdeville Y, Calder ES, Hibert C, Smith PJ, Cole P, LeFriant A (2015) Model space exploration for determining landslide source history from long-period seismic data. *Pure Appl Geophys* 172(2):389–413. <https://doi.org/10.1007/s00024-014-0852-5>
- Zhou J, Cui P, Hao M (2016) Comprehensive analyses of the initiation and entrainment processes of the 2000 Yigong catastrophic landslide in Tibet, China. *Landslides* 13 (1):39-54
- Zhou J, Cui P, Yang X (2013a) Dynamic process analysis for the initiation and movement of the Donghekou landslide-debris flow triggered by the Wenchuan earthquake. *Journal of Asian Earth Sciences* 76:70-84
- Zhou GGD, Cui P, Chen HY, Zhu XH, Tang JB, Sun QC (2013b) Experimental study on cascading landslide dam failures by upstream flows. *Landslides* 10 (5):633-643

Y. Yan · Z. Wang · S. Yin

Key Laboratory of High-speed Railway Engineering, MOE/School of Civil Engineering, Southwest Jiaotong University, Chengdu, 610031, China

Y. Yan

e-mail: yanyan1989@swjtu.edu.cn

Z. Wang

e-mail: ziang.wang@my.swjtu.edu.cn

S. Yin

e-mail: ysy.swjtu.edu.cn@my.swjtu.edu.cn

Y. Yan

Institute of Geographic Sciences and Natural Resources Research, Chinese Academy of Sciences, Beijing, 100101, China

Y. Cui (✉)

State Key Laboratory of Hydrosience and Engineering, Tsinghua University, Beijing, 100084, China
Email: yifeicui@mail.tsinghua.edu.cn

X. Tian

Institute of Geophysics, China Earthquake Administration, Beijing, 100081, China
e-mail: tianxin@cea-igp.ac.cn

S. Hu

College of Urban and Environmental Sciences, Northwest University, Xi'an, 710127, China
e-mail: shenghu@nwwu.edu.cn

J. Guo

Department of Geological Engineering, Chang'an University, Xi'an, 710054, China
e-mail: 2018026022@chd.edu.cn

L. Liao

Ecological Meteorology and Satellite Remote Sensing Center of Guizhou Province, Guiyang, 550002, China
e-mail: liufeng0208@126.com